

LETTER TO THE EDITOR

# Investigating aerosols as a reconciliation mechanism for K2-18 b JWST MIRI and NIRISS/NIRSpec observations

A. Y. Jaziri<sup>1,2</sup> and T. Drant<sup>3</sup>

<sup>1</sup> LATMOS/IPSL, UVSQ Université Paris-Saclay, Sorbonne Université, CNRS, Guyancourt, France

<sup>2</sup> Laboratoire d'astrophysique de Bordeaux, Univ. Bordeaux, CNRS, B18N, allée Geoffroy Saint-Hilaire, 33615 Pessac, France

<sup>3</sup> ETH University, Center for Origin and Prevalence of Life, Department of Earth and Planetary Sciences, 8092 Zurich, Switzerland.  
e-mail: yassin.jaziri@latmos.ipsl.fr

Received 19 August 2025; Accepted ??

## ABSTRACT

Recent JWST observations of the temperate sub-Neptune K2-18 b with NIRISS SOSS/NIRSpec G395H and MIRI LRS have yielded apparently inconsistent results: the MIRI spectra exhibit spectral features nearly twice as large as those seen at shorter wavelengths, challenging the high-metallicity, CH<sub>4</sub>-rich non-equilibrium model that fits the NIRISS/NIRSpec data. We perform a suite of atmospheric retrievals on both datasets, including free-chemistry, non-equilibrium, and aerosol models, using laboratory-derived complex refractive indices for a variety of photochemical haze analogues. Free retrievals systematically return lower metallicities than inferred by self-consistent chemical disequilibrium models, and the inclusion of absorbing aerosols, especially CH<sub>4</sub>-dominated, nitrogen-poor tholins, can further reduce the inferred metallicity by over an order of magnitude. These hazes reproduce the observed NIRISS slope through scattering and match MIRI features via C-H bending absorption near 7  $\mu\text{m}$ , while yielding particle properties consistent with photochemical production in H<sub>2</sub>-rich atmospheres. Although their inclusion improves the joint fit and reduces tension between datasets, it also significantly lowers the retrieved CH<sub>4</sub> abundance, highlighting degeneracies between metallicity, composition, and aerosol properties. Our results underscore the importance of aerosol absorption in interpreting temperate sub-Neptune spectra, and motivate future JWST observations and laboratory work to break these degeneracies.

**Key words.** exoplanets – atmospheres — aerosols – K2-18 b

## 1. Introduction

Recent observations with JWST NIRISS SOSS/NIRSpec G395H (Madhusudhan et al. 2023) and MIRI LRS (Madhusudhan et al. 2025) of the temperate sub-Neptune K2-18 b have sparked several debates regarding molecular detections and atmospheric characterization. The detection of CH<sub>4</sub> and CO<sub>2</sub> using NIRISS SOSS/NIRSpec G395H was initially reported by Madhusudhan et al. (2023), but the presence of CO<sub>2</sub> was later challenged and mitigated by Schmidt et al. (2025), before being recently confirmed by Hu et al. (2025). A comprehensive non-equilibrium study confirmed the detection of CH<sub>4</sub>, while also suggesting a high atmospheric metallicity ( $\sim 266$ ) and an elevated C/O ratio ( $\geq 2.1$ ) (Jaziri et al. 2025).

Subsequently, the MIRI LRS observations (Madhusudhan et al. 2025) reignited the discussion on molecular detections. However, these data yielded only marginal detection significance (Welbanks et al. 2025; Taylor 2025). A new reduction of the MIRI LRS data, combined with NIRISS SOSS/NIRSpec G395H observations (Luque et al. 2025), reached similar conclusions: a robust detection of CH<sub>4</sub>, while other molecular signatures remained statistically insignificant.

Nevertheless, one striking aspect of the MIRI LRS observations is the consistently higher amplitude of spectral features compared to those seen in the NIRISS SOSS/NIRSpec G395H data, regardless of the reduction method. These features, which formed the basis of claimed molecular detections in Madhusudhan et al. (2025), appear inconsistent across the full

set of observations. This can be seen in the joint analysis by Luque et al. (2025).

Given the apparent slope at shorter wavelengths in the NIRISS SOSS data and the high inferred abundance of methane (Madhusudhan et al. 2023, 2025; Hu et al. 2025), aerosols are likely present in the atmosphere of K2-18 b, such as methane clouds or photochemical hazes. Scattering-induced extinction by these atmospheric particles is known to flatten the spectra at shorter wavelengths without significantly affecting the longer wavelengths. They were for instance proposed to explain the flat spectra of the temperate sub-Neptune GJ 1214 b (Gao et al. 2023). The presence of photochemical hazes was also predicted in the simulations of Wogan et al. (2024) for K2-18 b. The absorption features observed in the K2-18 b MIRI LRS observations may be attributed to these hazes, reflecting the C-H bending resonances of the solid particles. In this work, we explore the role of aerosols in an effort to reconcile the various JWST observations of K2-18 b. All retrieval data can be downloaded from Zenodo<sup>1</sup>.

## 2. Methods

Using the MIRI LRS data reduced with Eureka! (Bell et al. 2022), from Luque et al. (2025), we performed atmospheric retrievals with TauREx 3<sup>2</sup> (Al-Refaie et al. 2021), including hydrocarbons as motivated by the non-equilibrium mod-

<sup>1</sup> <https://doi.org/10.5281/zenodo.16277833>

<sup>2</sup> <https://github.com/ucl-exoplanets/taurex3>

els of Jaziri et al. (2025). In combination with the NIRISS SOSS/NIRSpec G395H analysis from Jaziri et al. (2025), this approach aims to emphasize the discrepancies between the two datasets. While the results are data- and model-dependent, we provide here a consistent analysis with one retrieval code of a given set of reduced data, including in particular a complementary analysis of the MIRI LRS data reduced with Eureka!, which was not detailed in Luque et al. (2025).

We started by retrieving a flat spectrum to assess the statistical significance of any spectral features, for both dataset and combined dataset. Subsequently, we carried out retrievals including CH<sub>4</sub>, CO<sub>2</sub>, CO, H<sub>2</sub>O, NH<sub>3</sub>, C<sub>2</sub>H<sub>2</sub>, C<sub>2</sub>H<sub>4</sub>, H<sub>2</sub>CO, H<sub>2</sub>S, SO<sub>2</sub>, and HCN, which allowed us to identify the key absorbers for the combined analysis. We used absorption cross-sections computed by ExoMol (Yurchenko et al. 2011; Tennyson & Yurchenko 2012; Barton et al. 2013; Yurchenko et al. 2014; Barton et al. 2014), specifically those from Chubb et al. (2021).

We also carried out a retrieval including all molecules using the NIRISS SOSS/NIRSpec G395H data reduced with JExoRES (Madhusudhan et al. 2023) to derive a metallicity that is directly comparable through the same methodology. Additionally, we performed a non-equilibrium chemistry retrieval using TauREx 3 coupled with FRECKLL (Al-Refaie et al. 2024). While this approach remains computationally expensive and not yet fully stable, it was used to compare our results with non-equilibrium chemistry findings from the NIRISS SOSS/NIRSpec G395H data (Jaziri et al. 2025) and the consistency of the MIRI LRS observations under non-equilibrium conditions. These results are described in appendix C.

Additionally to the gray cloud parametrization used in all retrievals, we then used TauREx 3 together with the TauREx-PyMieScatt<sup>3</sup> module (Changeat et al. 2025) to retrieve the combined dataset, including aerosol contributions, and adopting a free-chemistry approach with a subset of relevant molecules selected based on retrievals performed without aerosols. An offset of -41 ppm between the NIRISS SOSS and NIRSpec G395H datasets was adopted from Madhusudhan et al. (2023). For the MIRI LRS dataset, an offset of +160 ppm was applied, determined by fitting it to the best retrieved non-equilibrium model from Jaziri et al. (2025) for the NIRISS SOSS/NIRSpec G395H data (see details in Appendix A).

The contribution of aerosols is accounted for using Mie scattering calculations. Previous strategies relied on the use of a simplified function to include aerosol scattering throughout the Rayleigh and Mie regimes (e.g., Kitzmann & Heng (2017)). This approach ignores the absorbing properties of the aerosols, encoded in the imaginary part of the complex refractive index, since absorption is usually negligible compared to scattering for small particles in the Visible and near-IR spectral range. In the present work, we include the absorbing properties of photochemical hazes that could explain the features observed in the K2-18 b observations at longer wavelengths in addition to the scattering effect at shorter wavelengths in the NIRISS SOSS/NIRSpec G395H range. The haze extinction is thus calculated using complex refractive index data obtained on laboratory haze analogues called tholins. The absorption properties of photochemical hazes are known to vary with the gas composition, temperature, pressure and irradiation efficiency (Brassé et al. 2015; Sciamma-O'Brien et al. 2023; Drant et al. 2024). We thus used 7 different datasets compiled from the original study of Khare et al. (1984) and the recent data of Drant et al. (2025) to

explore the influence of the haze absorbing properties on the retrieval and final posterior distribution. We performed simulations with the refractive index data of exoplanet haze analogs that were produced using two different experimental setups (PAMPRE at LATMOS and COSMIC at NASA Ames) using only CH<sub>4</sub> as a reactive gas. In addition, we performed simulations with the refractive index data obtained on Titan tholins using various experimental setups and N<sub>2</sub>/CH<sub>4</sub> ratio. The different refractive index data are summarized in Table 1. In the simulations, the haze particles are assumed spherical with a lognormal distribution in size. The particle radius is therefore the only microphysical parameter included in the retrieval. The consideration of fractal particles would increase the number of free parameters, e.g. with the fractal dimension and number of spherical monomers, produce other possibilities to explain the haze extinction and thus generally increase degeneracy (e.g., Adams et al. (2019)).

Table 1: Summary of the different haze refractive index data considered

Tholins	Gas composition	Experimental setup
exo1	95 % Ar - 5% CH <sub>4</sub>	PAMPRE
exo2	95 % Ar - 5% CH <sub>4</sub>	COSMIC
Titan1	90 % N <sub>2</sub> - 10% CH <sub>4</sub>	PAMPRE
Titan2	90 % N <sub>2</sub> - 10% CH <sub>4</sub>	COSMIC
Titan3	95 % N <sub>2</sub> - 5% CH <sub>4</sub>	PAMPRE
Titan4	95 % N <sub>2</sub> - 5% CH <sub>4</sub>	COSMIC
Titan5	90 % N <sub>2</sub> - 10% CH <sub>4</sub>	Khare et al. (1984)

See the priors and retrieval setup in Appendix B. We use the Bayes Factor (B), as defined in Benneke & Seager (2013), to assess the statistical significance of one model compared to another. This metric allows us to compare two models using their log-evidences (ln(Z)) and evaluate the relative significance of one retrieval compared to another. A value of ln(B) between 1 and 2.5 indicates weak preference, between 2.5 and 5 indicates moderate preference, and values above 5 indicate strong preference for one model over the other. However, these thresholds should be interpreted with caution, as recent work by Kipping & Benneke (2025) has shown that the strength of evidence may be less decisive than previously assumed.

### 3. Reconciling NIRISS SOSS/NIRSpec G395H and MIRI LRS observations with aerosols

Previous studies have retrieved high abundances of CH<sub>4</sub>, ranging from 1% to over 10% (Madhusudhan et al. 2023; Schmidt et al. 2025; Jaziri et al. 2025; Hu et al. 2025). Such significant methane levels suggest the formation of aerosols, such as Titan-like hazes via photochemistry (e.g., Trainer et al. (2006) and Arney et al. (2016)). Considering the modeled temperatures from previous studies (Charnay et al. 2021; Blain et al. 2021), along with our retrieved low temperatures, the formation of methane clouds is also plausible. These clouds may exhibit similar opacities to photochemical hazes generated in H<sub>2</sub>-dominated atmospheres. Both hazes and clouds could contribute to the flattening of the spectra at shorter wavelengths while preserving strong features at longer wavelengths. This could explain the differences in feature amplitudes observed between NIRISS SOSS/NIRSpec G395H and MIRI LRS observations.

In addition, photochemical hazes poor in nitrogen, as expected in H<sub>2</sub>-dominated sub-Neptune atmospheres, present significant absorption features attributed to C-H stretching (3.4 - 3.7

<sup>3</sup> <https://github.com/groningen-exoatmospheres/taurex-pymiescatt>

$\mu\text{m}$ ) and bending (6.7 - 7.2  $\mu\text{m}$ ) resonances (Drant et al. 2025) which partly overlap with the bands of gaseous methane and thus could be also one of the gases consistent with the K2-18 b observations. Similar absorption bands would also be expected for methane clouds making them also consistent with the observed absorption features.

The log-evidence results in Table 2 indicate a strong preference for all models compared to a flat line. This is driven by the NIRISS SOSS/NIRSpec G395H data, which have already been confirmed to contain significant spectral features, most notably  $\text{CH}_4$ . This is further supported by the retrieved metallicity, which remains consistent with values obtained using only NIRISS SOSS/NIRSpec G395H data (approximately 40 with a free-chemistry model).

We also observe that the combined analysis does not improve the  $\text{CO}_2$  detection, which is expected since  $\text{CO}_2$  has no noticeable feature in the mid-IR, and shows even less support for  $\text{C}_2\text{H}_4$  compared to retrievals based solely on MIRI LRS data.

Table 2: **Free** retrieval results for **combined** observations

Model	$\ln(Z)$	$\ln(B)$	metallicity
Flat line	28999.08	Reference	-
Worst model	29007.74	8.66	$21.07^{+18.48}_{-16.92}$
All molecules	29006.25	Reference	$40.85^{+8.49}_{-12.87}$
$\text{CH}_4/\text{C}_2\text{H}_4/\text{CO}_2$	29009.54	3.29	$19.63^{+14.53}_{-13.57}$
$\text{CH}_4/\text{C}_2\text{H}_4/\text{CO}_2$	29009.54	Reference	$19.63^{+14.53}_{-13.57}$
With Tholins exo1	29015.07	5.53	$0.29^{+1.27}_{-0.22}$
No $\text{CO}_2$	29007.74	1.84	$21.07^{+18.48}_{-16.92}$
With Tholins exo2	29011.21	1.67	$1.53^{+28.05}_{-1.46}$
With Tholins Titan1	29010.59	1.05	$2.14^{+30.89}_{-2.08}$
With Tholins Titan5	29010.27	0.73	$0.22^{+24.04}_{-0.18}$
With Tholins Titan2	29009.92	0.38	$20.64^{+15.51}_{-19.59}$
With Tholins Titan3	29009.76	0.07	$0.53^{+24.95}_{-0.48}$
With Tholins Titan4	29009.47	-0.07	$26.74^{+13.20}_{-12.64}$
No $\text{C}_2\text{H}_4$	29009.68	-0.14	$14.71^{+17.30}_{-11.64}$

For the tholins retrievals, the log-evidence values in Table 2 reveal discrepancies depending on the specific tholins data used. These discrepancies are explained by the variability in the strength and position of absorption features between the different datasets. One dataset in particular, tholins exo1, is strongly favored. Unlike the others, except for tholins exo2, tholins exo1 lacks features associated with nitrogen bonds and instead shows only  $-\text{CH}_x$  signatures. The tholins exo2, although produced from a similar gas composition, exhibits  $\text{C}=\text{C}$  absorption features which are not observed in the K2-18 b observations. Only the  $\text{C}-\text{H}$  haze features of the tholins exo1 are consistent with the observed spectral features, especially the  $7\mu\text{m}$  band previously attributed to DMS and DMDS by Madhusudhan et al. (2025). The contributions of the various tholins datasets to the retrieved spectra are shown in Figure 1, highlighting the spectral specificity of tholins exo1. The different Titan tholins datasets, including the one of Khare et al. (1984) used in the previous work of Wogan et al. (2024), are not as favored as exo1 which is explained by the stronger absorbing power of these hazes produced in  $\text{N}_2$ -rich gas mixtures and the different  $\text{N}-\text{H}$ ,  $\text{C}\equiv\text{N}$ ,  $\text{C}=\text{N}$  absorption features which are not consistent with the K2-18 b observations. This analysis emphasizes the importance of the haze

refractive index, especially the imaginary part of the refractive index that reflects absorption, since it influences the retrieval and can help rule out some haze composition based on the observed features at longer wavelengths.

The best-fit model includes tholins exo1 and is preferred over models without tholins, though the preference is at the threshold between strong and moderate significance. The spectrum and its contributions are shown in Figure D.1, illustrating two key points:

**Increased scale height:** Compared to retrievals without tholins, the atmosphere's base appears at a lower transit depth, decreasing from  $\sim 0.0028$  to  $\sim 0.0025$ . This corresponds to a significantly lower retrieved metallicity, dropping from 19.63 to 0.29, relative to the reference retrieval (see Table 2). This reflects the well-known degeneracy between cloud-top pressure and atmospheric metallicity. It also leads to a substantially lower retrieved  $\text{CH}_4$  abundance, reduced by about two orders of magnitude (see Figure D.4 and D.3).

**Tholins spectral contribution:** Tholins exo1 contributes to the observed features across multiple spectral ranges: near  $7\mu\text{m}$  in the MIRI LRS range and around  $3.4\mu\text{m}$  in the NIRSpec G395H range (alongside  $\text{CH}_4$ ) as absorption dominates, and at shorter wavelengths in the NIRISS SOSS range, affecting the spectral slope as scattering dominates. Notably, the retrieved  $\text{CH}_4$  abundance decreases from  $6.3\times 10^{-2}$  to  $3.0\times 10^{-4}$  when considering these photochemical hazes compared to the reference model. The haze properties retrieved are also reasonable and in agreement with the modeling predictions of Lavvas et al. (2019) made for the temperature sub-Neptune GJ 1214 b. For the retrieval considering exo1 tholins, we constrain the particle radius in log unit to  $-1.65^{+0.09}_{-0.12}$  (in  $\mu\text{m}$ ), the haze density in log unit to  $11.22^{+0.36}_{-0.36}$  ( $\text{m}^{-3}$ ), the mean pressure of the haze layer in log unit to  $-0.04^{+1.02}_{-0.98}$  (in Pa), and the dP of the haze layer in log unit to  $2.05^{+1.06}_{-0.87}$  (in Pa), see Figure D.3. The retrievals considering hazes also tend to increase the atmospheric temperature (see Figure D.2) which along with the haze properties and the methane abundance affects the strength of the spectral features. Although this result reflects a degenerate behavior between different parameters influencing extinction, its physical meaning is reasonable as haze absorption in the UV-Visible tend to increase the atmospheric temperature of the upper atmosphere (e.g., Arney et al. 2016)). This increased temperature driven by the haze heating properties could inhibit the formation of methane clouds and prevent the co-existence with the solid organic hazes.

While the spectral fit is broadly consistent when considering photochemical hazes, the resulting decrease in the retrieved  $\text{CH}_4$  abundance goes against the initial motivation for considering their presence. The presence of photochemical hazes produced from gaseous methane is however generally consistent with the current data.

## 4. Conclusions

We have investigated the apparent inconsistency between JWST NIRISS SOSS/NIRSpec G395H and MIRI LRS transmission spectra of the temperate sub-Neptune K2-18 b. The MIRI LRS observations exhibit apparent spectral features with amplitudes roughly twice those seen in the NIRISS SOSS/NIRSpec G395H data, which cannot be reproduced by the high-metallicity non-equilibrium model that fits the shorter-wavelength observations.

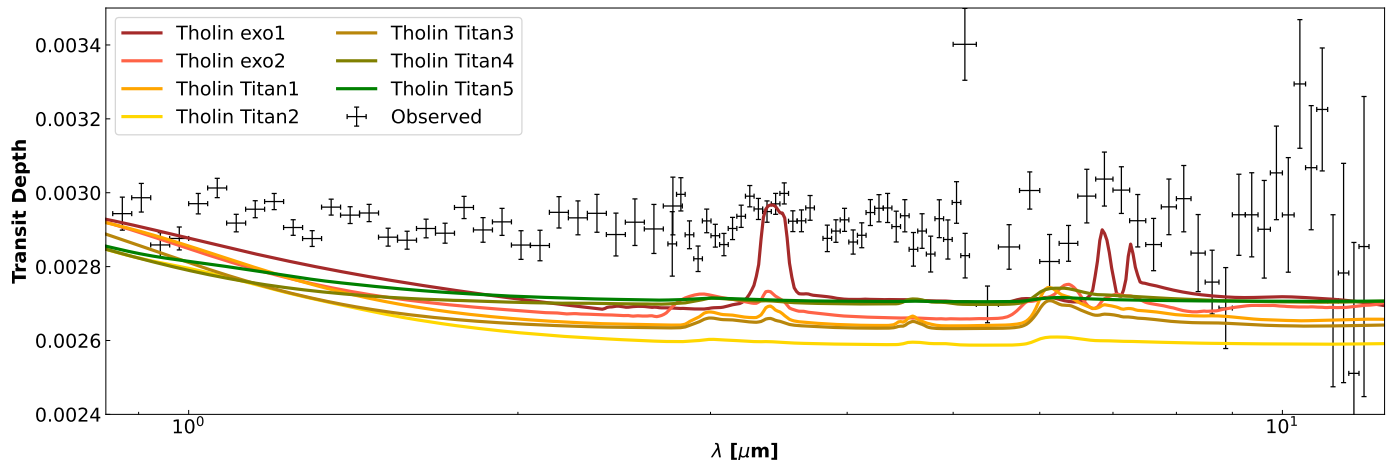


Fig. 1: Combined spectra of NIRISS SOSS/NIRSpec G395H low resolution (Madhusudhan et al. 2023) and MIRI LRS Eureka! data reduction (Luque et al. 2025) (error bars) are shown alongside the retrieved tholins contributions (solid lines) of the different tholins data for each corresponding combine retrieval.

Free-chemistry and non-equilibrium retrievals on the MIRI LRS spectrum instead favor lower metallicities and molecular compositions that are inconsistent with the NIRISS/NIRSpec results, yet none of the tested molecular models are statistically preferred over a flat spectrum for MIRI LRS alone.

To reconcile the datasets, we explored the role of aerosols, specifically photochemical hazes and methane clouds, which can flatten spectra at shorter wavelengths while preserving or enhancing features at longer wavelengths. Using laboratory-derived complex refractive indices for a range of haze analogues, we find that only hazes produced in  $\text{CH}_4$ -dominated mixtures without nitrogen and C=C features (tholins exo1) yield absorption signatures consistent with the combined NIRISS, NIRSpec, and MIRI data. These hazes naturally reproduce the observed slope in the NIRISS SOSS range through scattering, while contributing C-H bending absorption features near 7  $\mu\text{m}$  in the MIRI LRS range.

The inclusion of such hazes improves the combined fit and moderately reduces the tension between the two datasets, though at the cost of significantly lowering the retrieved  $\text{CH}_4$  abundance. The retrieved haze particle sizes, number densities, and layer pressures are broadly consistent with theoretical predictions for  $\text{H}_2$ -dominated sub-Neptune atmospheres, and the associated temperature increases in the upper atmosphere are physically plausible given aerosol absorption in the optical.

Overall, our results highlight the importance of aerosol absorption, particularly the imaginary component of the refractive index, in interpreting the atmospheres of temperate sub-Neptunes. While photochemical hazes offer a promising explanation for the discrepancy between short- and long-wavelength observations of K2-18 b, the current data do not yet allow a definitive determination of their composition or abundance. Future JWST observations and higher precision, alongside expanded laboratory measurements of exoplanet haze analogues, will be essential to break degeneracies between metallicity, molecular composition, and aerosol properties.

**Acknowledgements.** This project has received funding from the European Research Council (ERC) under the ERC OxyPlanets projects (grant agreement No. 101053033). This project acknowledges funding from the European Research Council (ERC) under the European Union’s Horizon 2020 research and innovation programme (grant agreement No. 679030/WHIPLASH). T.D. acknowledges support by the 2024 NOMIS-ETH postdoc fellowship program. T.D. thanks the

NOMIS foundation and ETH Zurich for funding via the 2024 Fellowship program.

## References

- Adams, D., Gao, P., de Pater, I., & Morley, C. 2019, ApJ, 874
- Al-Refai, A. F., Changeat, Q., Waldmann, I. P., & Tinetti, G. 2021, ApJ, 917, 37
- Al-Refai, A. F., Venot, O., Changeat, Q., & Edwards, B. 2024, ApJ, 967, 132
- Arney, G. N., Domagal-Goldman, S. D., Meadows, V. S., et al. 2016, Astrobiology, 16, 873
- Barton, E. J., Chiu, C., Golpayegani, S., et al. 2014, MNRAS, 442, 1821
- Barton, E. J., Yurchenko, S. N., & Tennyson, J. 2013, MNRAS, 434, 1469
- Bell, T., Ahrer, E.-M., Brande, J., et al. 2022, The Journal of Open Source Software, 7, 4503
- Benneke, B. & Seager, S. 2013, ApJ, 778, 153
- Blain, D., Charnay, B., & Bézard, B. 2021, A&A, 646, A15
- Brassé, C., Muñoz, O., Coll, P., & Raulin, F. 2015, Planetary and Space Science, 109–110, 159
- Changeat, Q., Bardet, D., Chubb, K., et al. 2025, arXiv e-prints, arXiv:2505.18715
- Charnay, B., Blain, D., Bézard, B., et al. 2021, A&A, 646, A171
- Chubb, K. L., Rocchetto, M., Yurchenko, S. N., et al. 2021, A&A, 646, A21
- Drant, T., Garcia-Caurel, E., Perrin, Z., et al. 2024, A&A, 682, A6
- Drant, T., Sciamma-O’Brien, E., Jovanovic, L., et al. 2025, A&A in review
- Gao, P., Piette, A. A. A., Steinrueck, M. E., et al. 2023, The Astrophysical Journal, 951, 96
- Gao, P., Wakeford, H., Moran, S., & Parmentier, V. 2021, JGR Planets, 126
- Hu, R., Bello-Arufe, A., Tokadjian, A., et al. 2025, arXiv e-prints, arXiv:2507.12622
- Jaziri, A. Y., Sohier, O., Venot, O., & Carrasco, N. 2025, A&A, 701, 12
- Khare, B. N., Sagan, C., Arakawa, E. T., et al. 1984, Icarus, 60, 127
- Kipping, D. & Benneke, B. 2025, arXiv e-prints, arXiv:2506.05392
- Kitzmann, D. & Heng, K. 2017, MNRAS, 475, 94
- Lavvas, P., Koskinen, T., Steinrueck, M. E., García Muñoz, A., & Showman, A. P. 2019, The Astrophysical Journal, 878, 118
- Luque, R., Piaulet-Ghorayeb, C., Radica, M., et al. 2025, arXiv e-prints, arXiv:2505.13407
- Madhusudhan, N., Constantinou, S., Holmberg, M., et al. 2025, ApJ, 983, L40
- Madhusudhan, N., Sarkar, S., Constantinou, S., et al. 2023, ApJ, 956, L13
- Schmidt, S. P., MacDonald, R. J., Tsai, S.-M., et al. 2025, arXiv e-prints, arXiv:2501.18477
- Sciamma-O’Brien, E., Roush, T. L., Rannou, P., Dubois, D., & Salama, F. 2023, The Planetary Science Journal, 4, 121
- Taylor, J. 2025, Research Notes of the American Astronomical Society, 9, 118
- Tennyson, J. & Yurchenko, S. N. 2012, MNRAS, 425, 21
- Trainer, M., Pavlov, A., DeWitt, H., et al. 2006, PNAS, 103, 18035
- Welbanks, L., Nixon, M. C., McGill, P., et al. 2025, arXiv e-prints, arXiv:2504.21788
- Wogan, N. F., Batalha, N. E., Zahnle, K. J., et al. 2024, The Astrophysical Journal Letters, 963, L7
- Yurchenko, S. N., Barber, R. J., & Tennyson, J. 2011, MNRAS, 413, 1828
- Yurchenko, S. N., Tennyson, J., & Bailey, J. e. a. 2014, Proceedings of the National Academy of Science, 111, 9379

## Appendix A: Dataset offset

Using different telescope instruments can introduce biases between datasets, such as flux offsets. In this study, we work with three JWST datasets obtained from three different instruments: NIRISS SOSS, NIRSpec G395H, and MIRI LRS. For the NIRISS SOSS and NIRSpec G395H data, we use the observations from [Madhusudhan et al. \(2023\)](#), along with their reported offset of  $-41$  ppm. The MIRI LRS data are taken from the Eureka! reduction from [Luque et al. \(2025\)](#), who found a flux offset ranging from approximately  $+120$  ppm to  $+160$  ppm depending on their retrieval priors or retrieval code.

To ensure consistency with the non-equilibrium modeling results from [Jaziri et al. \(2025\)](#), we use their best-fitting model to determine the optimal offset for the MIRI LRS dataset via a  $\chi^2$  minimization approach. The resulting  $\chi^2$  values as a function of the wavelength shift are shown in Figure A.1, along with a second-order polynomial fit. The minimum  $\chi^2$  corresponds to an offset of  $+160$  ppm, which we adopt for this study.

All these offsets are fixed to reduce the parameter space and accelerate aerosol retrievals. Allowing them to vary would affect the precise values of the retrieved parameters but not the main conclusions regarding the impact of aerosols on the spectra.

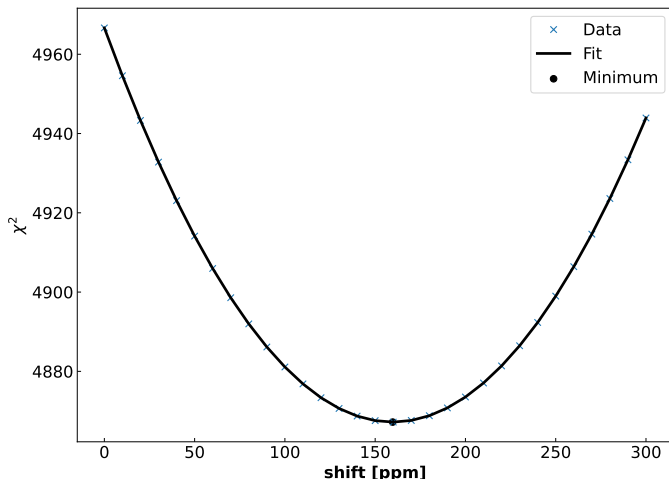


Fig. A.1: The  $\chi^2$  of the best non-equilibrium model from [Jaziri et al. \(2025\)](#) is shown as a function of the MIRI LRS wavelength shift, based on the combined JWST observations from NIRISS SOSS, NIRSpec G395H ([Madhusudhan et al. 2023](#)), and MIRI LRS ([Luque et al. 2025](#)). Blue cross markers indicate the computed values, and a second-order polynomial fit is shown as a black solid line, with its minimum value (160 ppm) marked by a black dot.

## Appendix B: Retrieval setup

We performed four types of retrievals: flat-line, non-equilibrium chemistry, and constant-chemistry (with and without aerosols).

The flat-line retrieval was conducted by retrieving the planetary radius and a cloud deck, following the priors listed in Table B.1. A minimal amount of  $\text{H}_2\text{O}$  (between  $10^{-12}$  and  $10^{-11}$ ) was included, as TauREx 3 requires at least one absorber to run. The radius and the cloud deck are also retrieved for all other retrievals following the same priors.

For all other retrievals, the temperature profile was parameterized with 4-points. This is the minimum required to allow

for a thermal inversion, capture deep-atmosphere temperatures relevant to disequilibrium chemistry and quenching processes, and assess aerosol impacts on the upper-atmosphere temperature. Temperature priors are detailed in Table B.1.

The non-equilibrium chemistry retrieval was carried out using FRECKLL coupled with TauREx 3, without aerosols.  $K_{zz}$  has been set to  $10^{10}$ . Its value, within common range of values, has been shown in [Jaziri et al. \(2025\)](#) to not significantly affect the retrieval. The priors are detailed in Table B.1. Due to its high computational cost and limited stability, we present only one non-equilibrium retrieval, applied to the MIRI LRS data, which contain relatively few data points. This allows us to assess the consistency of the MIRI LRS observations under non-equilibrium conditions.

We then used vertically constant profiles for the chemical species (commonly referred to as free chemistry), including all the molecules listed in Table B.1, with their corresponding priors, for retrievals on the MIRI LRS data. This set of molecules represents the main species of interest that have been highlighted in the literature and are available in the ExoMol database, which is the most relevant source for opacities calculated for  $\text{H}_2$ -dominated atmospheres. Each molecule was removed individually to assess its significance compared to the reference case with all molecules. A subset of the most significant molecules was then selected to reduce computational cost in subsequent retrievals that include aerosols, which are more expensive to model. The aerosol priors are also provided in Table B.1. This optimized subset of molecules was then used for retrievals of combined NIRISS SOSS, NIRSpec G395H, and MIRI LRS data, both with and without aerosols, using the same set of priors.

## Appendix C: Inconsistency between NIRISS SOSS/NIRSpec G395H and MIRI LRS observations

The NIRISS SOSS/NIRSpec G395H data exhibit feature amplitudes of approximately 200 ppm, whereas the MIRI LRS data show features at least twice as large. The relatively small amplitudes in the NIRISS SOSS/NIRSpec G395H data have been shown to favor high metallicity, with a value of 266 inferred using a non-equilibrium chemical model ([Jaziri et al. 2025](#)). However, the best-fit non-equilibrium model, using a grid of forward models with FRECKLL, from [Jaziri et al. \(2025\)](#) appears inconsistent with the larger spectral amplitudes seen in the MIRI LRS data, as illustrated in Figure C.1.

When applying a free-chemistry retrieval to the MIRI LRS data, we are able to fit the larger spectral features. The log-evidence results in Table C.1 indicate that the three most favored molecules are  $\text{C}_2\text{H}_2$ ,  $\text{H}_2\text{CO}$ , and  $\text{C}_2\text{H}_4$ . These molecules have absorption bands that align with the apparent features in the MIRI LRS spectrum, as shown in Figure C.1, where the best-fit model is overplotted on the observations. The retrieved metallicity is significantly lower, with a maximum value of  $4.42^{+14.31}_{-4.06}$ , compared to the value of 266 reported by [Jaziri et al. \(2025\)](#). It is important to note that [Jaziri et al. \(2025\)](#) used a non-equilibrium chemical model.

A retrieval using all molecules on the NIRISS SOSS/NIRSpec G395H data yields a metallicity of  $40.56^{+9.62}_{-13.35}$ , demonstrating that, in our case, free-chemistry retrievals tend to bias metallicities toward lower values compared to non-equilibrium models. This bias arises from missing molecules, such as  $\text{CO}$  or  $\text{N}_2$ , that may be abundant but have no prominent spectral features, and therefore cannot be well-constrained in the

Table B.1: Free parameters and priors for the retrievals.

Parameters	Bounds
<b>Common</b>	
$T_{top}$ [K]	50 to 700
$T_{bot}$ [K]	300 to 1000
$T_1$ [K]	50 to 700
$T_2$ [K]	50 to 700
$\log_{10}(P_1)$ [Pa]	2 to 6
$\log_{10}(P_2)$ [Pa]	-1 to 5
$\log_{10}(P_{clouds})$ [Pa]	-2 to 6
radius [ $R_{Jup}$ ]	0.1 to 0.3
<b>Chemistry</b>	
<b>Non-equilibrium</b>	
$\log(Z)$	-2 to 3
C/O	0.01 to 10.0
<b>Constant</b>	
$\log_{10}(H_2O)$	-12 to -1
$\log_{10}(CO)$	-12 to -1
$\log_{10}(CH_4)$	-12 to -0.15
$\log_{10}(CO_2)$	-12 to -1
$\log_{10}(HCN)$	-12 to -1
$\log_{10}(NH_3)$	-12 to -1
$\log_{10}(C_2H_2)$	-12 to -1
$\log_{10}(C_2H_4)$	-12 to -1
$\log_{10}(H_2CO)$	-12 to -1
$\log_{10}(SO_2)$	-12 to -1
$\log_{10}(H_2S)$	-12 to -1
<b>Aerosols</b>	
$\log(\mu)$ [ $\mu m$ ]	-2 to 1
$\log(\chi)$ [molecules.m $^{-3}$ ]	4 to 13
$\log(P)$ [Pa]	-2 to 5
$\log(\Delta P)$ [Pa]	-1 to 5

retrieval. Nevertheless, the MIRI LRS retrievals tend to favor lower metallicity to increase the scale height, allowing better fits to the larger observed features. This conclusion is valid because  $CH_4$  is the dominant gas.

These results are inconsistent with those from the NIRISS SOSS/NIRSpec G395H analysis and the non-equilibrium chemical model, both of which favor higher metallicity and a high  $CH_4$  abundance, as seen in Figure C.1. In contrast, the MIRI LRS retrievals indicate low metallicity and do not show a preference for  $CH_4$ . However, as shown in Table C.1, none of the tested models are statistically favored over a flat line. At best, they fall within the "weak preference" range.  $H_2CO$  is unlikely to be dominant. Its retrieved abundance of  $10^{-5}$  exceeds the  $3\sigma$  upper limit derived by Jaziri et al. (2025).  $C_2H_2$  and  $C_2H_4$  could plausibly be present, especially considering high C/O ratio and high metallicity. However, the retrievals favor  $C_2H_2$  over  $CH_4$ , which is inconsistent with the NIRISS SOSS/NIRSpec G395H data.

For the combined analysis, we therefore adopted  $CH_4$ ,  $C_2H_4$ , and  $CO_2$  as the key molecules.  $CO_2$  remains somewhat uncertain in the NIRISS SOSS/NIRSpec G395H data, but was included for completeness since it has been recently confirmed with the new data from Hu et al. (2025).

Finally, a non-equilibrium chemistry retrieval on the MIRI LRS data reveals that the feature amplitudes are inconsistent with such models. The solution shows bimodality (see Figure C.2), with one mode corresponding to a low radius ( $0.2173^{+0.0007}_{-0.0006} R_{Jup}$ ) and low metallicity ( $0.04^{+0.35}_{-0.02}$ ) to produce a high scale height, and the other corresponding to a higher ra-

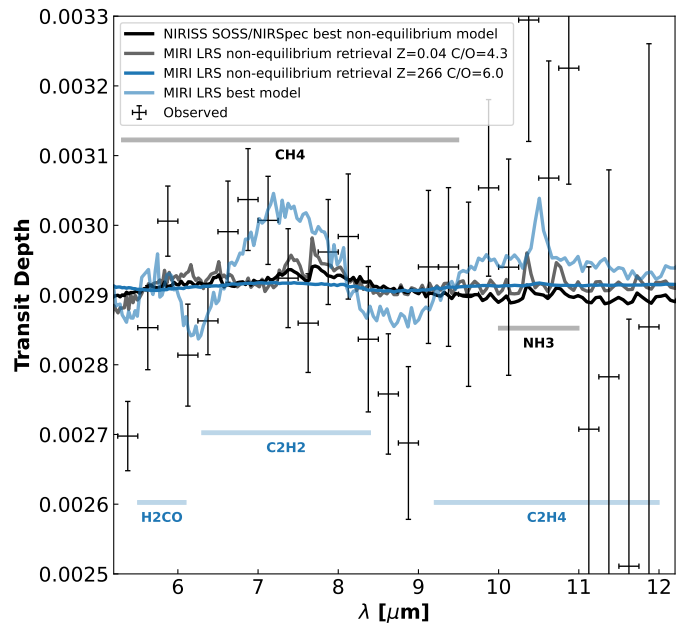


Fig. C.1: Spectrum from the MIRI LRS Eureka! data reduction (Luque et al. 2025) (error bars) is compared to the best non-equilibrium model from Jaziri et al. (2025) (black solid line), which fits the NIRISS SOSS/NIRSpec G395H observations. They are also compared to the two MIRI LRS non-equilibrium retrieval solutions (light black solid line for low metallicity and blue solid line for high metallicity), as well as to the best MIRI LRS model (light blue solid line), all shown at a resolution of 200. Key spectral features are highlighted in their respective colors.

dius ( $0.2245^{+0.0006}_{-0.0009} R_{Jup}$ ) and high metallicity ( $266^{+243}_{-125}$ ). In the high-metallicity case, a higher C/O ratio ( $> 3.5$ ) is also preferred, which enhances  $C_2H_2$  and  $C_2H_4$  features, similar to the free retrieval, but makes the result inconsistent with the NIRISS SOSS and NIRSpec G395H data that favor  $CH_4$  and  $NH_3$  features (see Figure C.1). Higher temperatures ( $> 340$  K) are also favored. The feature amplitudes appear smaller compared to the data, although this mismatch is somewhat reduced in the low-metallicity scenario where  $CH_4$  is dominant. Nonetheless, the feature amplitudes remain smaller than those predicted by the free-chemistry retrieval and the observed amplitudes (see Figure C.1).

Since none of the models are statistically significant, we cannot draw definitive conclusions, but these inconsistencies suggest that a key process may be missing from our current models.

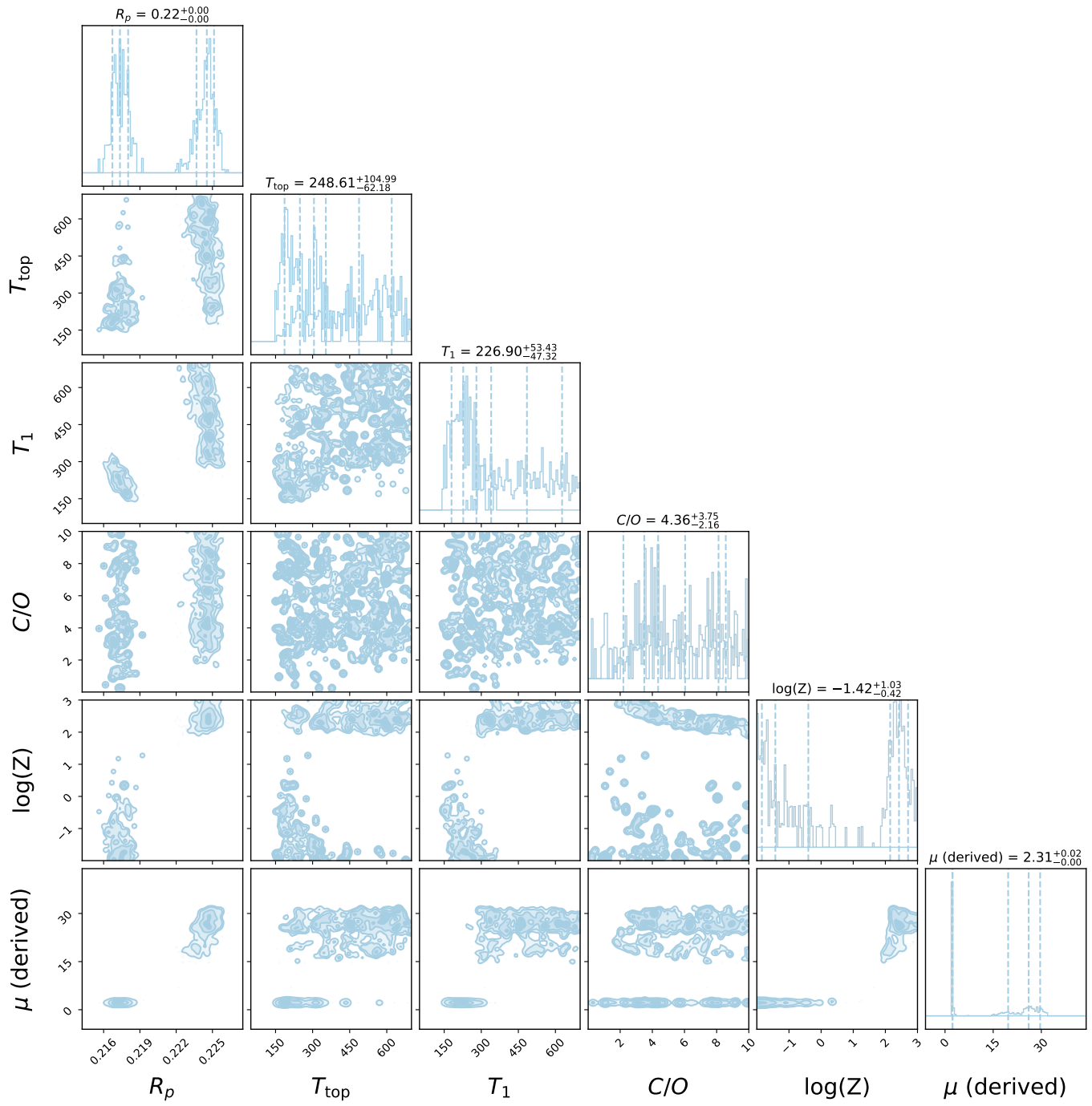


Fig. C.2: Corner plot of the non-equilibrium retrieval model with FRECKLL on the MIRI LRS Eureka! data reduction (Luque et al. 2025).

Table C.1: Retrieval results for MIRI LRS

Model	ln(Z)	ln(B)	metallicity
Flat line	185.11	Reference	-
Best model	187.56	2.45	$0.28^{+4.72}_{-0.27}$
All molecules	186.93	Reference	$4.41^{+13.98}_{-4.02}$
No C <sub>2</sub> H <sub>2</sub>	185.90	1.03	$4.42^{+14.31}_{-4.06}$
No H <sub>2</sub> CO	186.08	0.85	$4.28^{+15.60}_{-3.96}$
No C <sub>2</sub> H <sub>4</sub>	186.36	0.57	$2.43^{+12.66}_{-2.28}$
No HCN	186.75	0.18	$2.82^{+12.92}_{-2.59}$
No CO	186.78	0.15	$4.14^{+14.61}_{-3.80}$
No CH <sub>4</sub>	186.85	0.08	$2.73^{+12.41}_{-2.52}$
No CO <sub>2</sub>	186.86	0.07	$3.20^{+12.14}_{-2.94}$
No NH <sub>3</sub>	186.90	0.03	$3.21^{+13.83}_{-2.99}$
No H <sub>2</sub> O	186.91	0.02	$3.55^{+14.42}_{-3.24}$
No H <sub>2</sub> S	186.91	0.02	$3.50^{+12.58}_{-3.18}$
No SO <sub>2</sub>	187.21	-0.28	$3.41^{+13.34}_{-3.10}$
CH <sub>4</sub> /C <sub>2</sub> H <sub>2</sub> /C <sub>2</sub> H <sub>4</sub> H <sub>2</sub> O/H <sub>2</sub> CO	187.26	Reference	$0.62^{+6.66}_{-0.59}$
No C <sub>2</sub> H <sub>2</sub>	186.15	1.11	$0.33^{+6.24}_{-0.32}$
No H <sub>2</sub> CO	186.51	0.75	$0.34^{+5.54}_{-0.33}$
No C <sub>2</sub> H <sub>4</sub>	186.51	0.75	$0.04^{+1.23}_{-0.03}$
No H <sub>2</sub> O	187.24	0.02	$0.19^{+3.47}_{-0.18}$
No CH <sub>4</sub>	187.56	-0.30	$0.28^{+4.72}_{-0.27}$
With Tholins exo1	186.83	-0.43	$1.26^{+7.82}_{-1.19}$

## Appendix D: Joint NIRISS SOSS/NIRSpec G395H and MIRI LRS data additional materials

In this appendix, we present Figure D.1 and Figure D.3 respectively the spectral contributions and the corner plot of the best-fit model from the joint NIRISS SOSS/NIRSpec G395H and MIRI LRS retrieval, as well as the temperature profiles from two retrievals Figure D.2, with and without haze, to illustrate the effect of haze on the retrieved temperature, as discussed in Section 3. Figure D.4 show the corner plot of free retrieval model with  $\text{CH}_4/\text{C}_2\text{H}_4/\text{CO}_2$  on the combine spectra. Figure D.4 show the corner plot of free retrieval model with  $\text{CH}_4/\text{C}_2\text{H}_4/\text{CO}_2$  on the combine spectra. Our retrieved temperatures in Figure D.2 are generally higher than the condensation curve for methane (see Fig 1 of [Gao et al. \(2021\)](#) for example) which may suggest that photochemical hazes are a more likely aerosol candidate than methane clouds to reconcile the K2-18 b JWST observations.

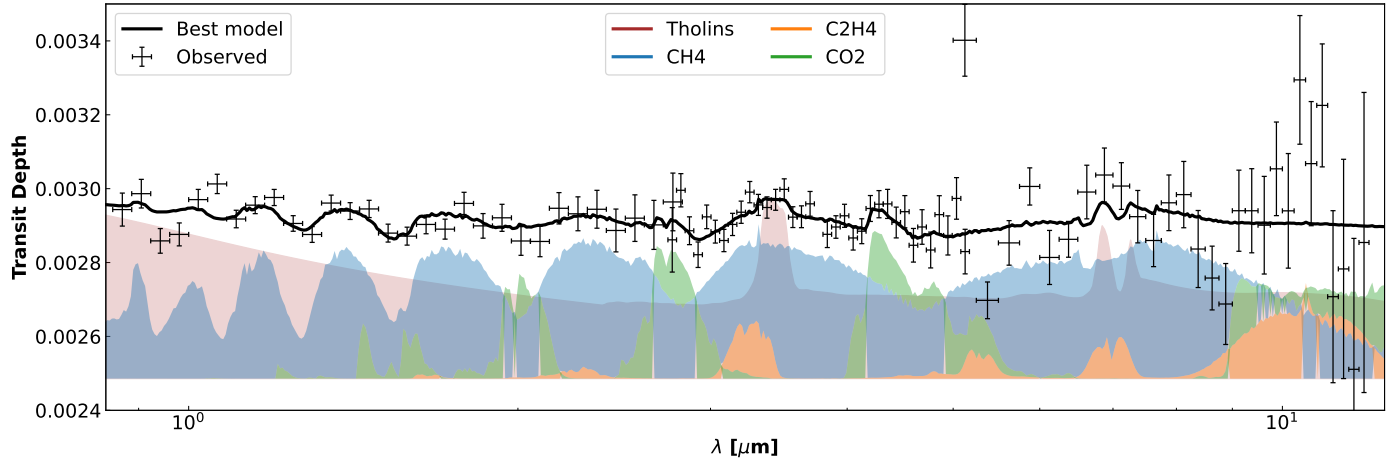


Fig. D.1: Combined spectra of NIRISS SOSS/NIRSpec G395H low resolution ([Madhusudhan et al. 2023](#)) and MIRI LRS Eureka! data reduction ([Luque et al. 2025](#)) (error bars) are shown alongside the best model (black solid line) and its contributions. It correspond to the retrieval including tholins exo1.

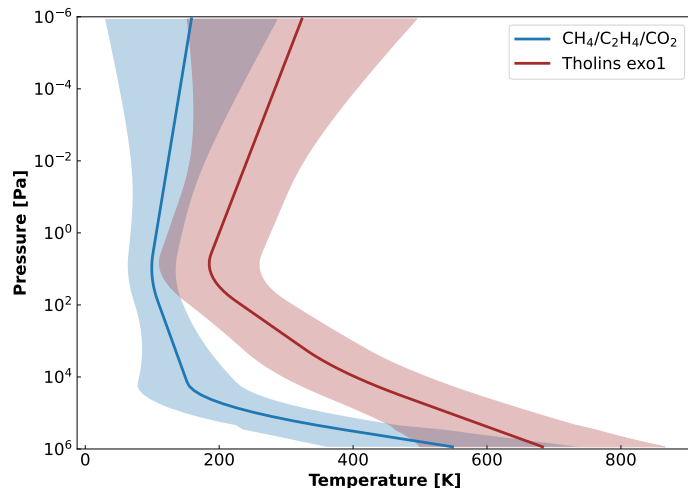


Fig. D.2: Retrieved temperature profile with its uncertainty from the retrieval using  $\text{CH}_4/\text{C}_2\text{H}_4/\text{CO}_2$  (blue) and with the addition of tholins exo1 (brown), based on the combined observations.

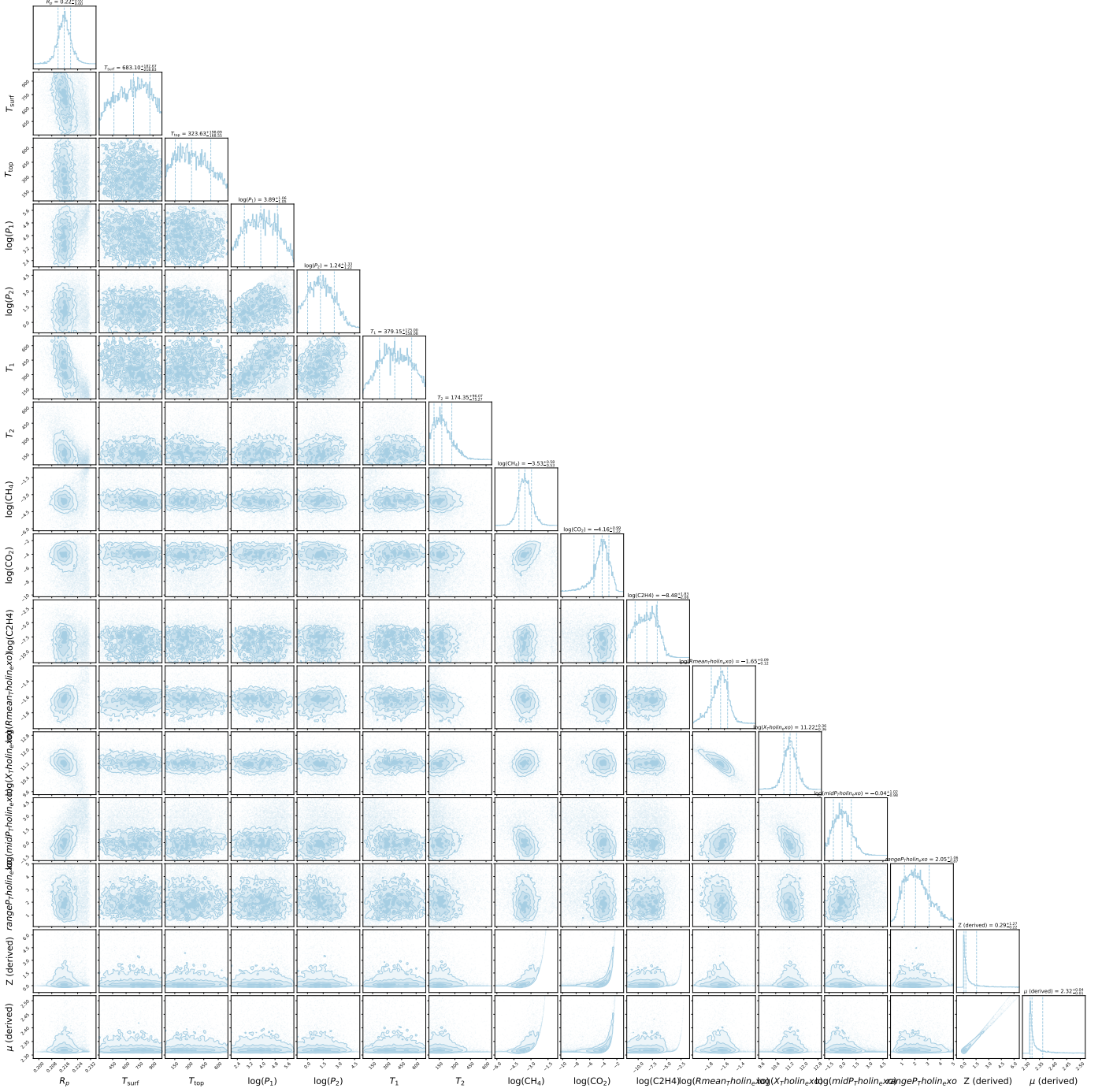


Fig. D.3: Corner plot of the best retrieval model on the combined spectra of NIRISS SOSS/NIRSpec G395H (Madhusudhan et al. 2023) and MIRI LRS Eureka! data reduction (Luque et al. 2025). It corresponds to the retrieval including tholins exo1.

